Nanoscale

ROYAL SOCIETY OF CHEMISTRY

PAPER

Cite this: *Nanoscale*, 2021, **13**, 16543

One-step hydrothermal synthesis of porous $Ti_3C_2T_z$ MXene/rGO gels for supercapacitor applications†

Sanjit Saha,[a] Kailash Arole,[b] Miladin Radovic,[b] Jodie L. Lutkenhaus *[a,b] and Micah J. Green *[a,b]

Received 5th April 2021,
Accepted 6th September 2021

DOI: 10.1039/d1nr02114a

rsc.li/nanoscale

Titanium carbide/reduced graphene oxide ($Ti_3C_2T_z$/rGO) gels were prepared by a one-step hydrothermal process. The gels show a highly porous structure with a surface area of ~224 m^2 g^{-1} and average pore diameter of ~3.6 nm. The content of GO and $Ti_3C_2T_z$ nanosheets in the reaction precursor was varied to yield different microstructures. The supercapacitor performance of $Ti_3C_2T_z$/rGO gels varied significantly with composition. Specific capacitance initially increased with increasing $Ti_3C_2T_z$ content, but at high $Ti_3C_2T_z$ content gels cannot be formed. Also, the retention of capacitance decreased with increasing $Ti_3C_2T_z$ content. $Ti_3C_2T_z$/rGO gel electrodes exhibit enhanced supercapacitor properties with high potential window (1.5 V) and large specific capacitance (920 F g^{-1}) in comparison to pure rGO and $Ti_3C_2T_z$. The synergistic effect of EDLC from rGO and redox capacitance from $Ti_3C_2T_z$ was the reason for the enhanced supercapacitor performance. A symmetric two-electrode supercapacitor cell was constructed with $Ti_3C_2T_z$/rGO, which showed very high areal capacitance (158 mF cm^{-2}), large energy density (~31.5 μW h cm^{-2} corresponding to a power density of ~370 μW cm^{-2}), and long stability (~93% retention) after 10 000 cycles.

1. Introduction

The development of novel supercapacitor-electrode materials is necessary for advancing energy storage technology, particularly if intermittent renewable energy sources are being used.[1,2] Supercapacitors in particular have attracted extensive attention due to their high-power density and long cycle-life. Depending on the charge storage mechanism, supercapacitors can be classified into two groups. First, capacitors with electrochemical double layer capacitance (EDLC) where carbonaceous materials like graphene, reduced graphene oxide (rGO) and CNT store charges by forming a double layer at the material–electrolyte interface.[3] Second, redox capacitance devices store charge by faradaic reaction.[3] A redox or pseudocapacitive material can store more charge per unit mass than EDLC materials. However, metal oxides exhibit poor electronic conductivity, and conductive polymers have low structural stability. These drawbacks of common redox materials restricts their practical application in supercapacitor electrodes.[4] New materials are needed to address this problem.

The recent discovery of two-dimensional carbides and nitrides, referred to as MXenes, are promising for supercapacitor electrodes due to their properties and 2-D geometry. MXenes are typically derived from MAX phases, where M represents early transition metals (Ti, V, and Nb *etc.*), A is an element from the groups 13–16, and X stands for carbon or nitrogen. MXenes possess three unique properties: (i) the transition metal M has a variable oxidation state which increases the charge transfer;[5] (ii) the functional groups at MXene surfaces are redox active,[6] and (iii) they facilitate fast ion transport due to the stacked structure.[7] The T_z in MXenes with general formula $M_{n+1}X_nT_z$ represents the surface groups such as –F, –O, and –OH. These functional groups produce a high capacitance in aqueous electrolytes.[8] Moreover, the oxidation state of titanium is changed in H_2SO_4, due to the protonation of oxygen functional groups with the intercalated H^+. However, re-stacking of MXene layers can deteriorate the charge storage efficiency by preventing full use of electrochemically active sites. In addition, $Ti_3C_2T_z$ has restricted potential windows (<1 V), which decreases the energy density of supercapacitor.[9]

To overcome these limitations, hybrid structures of MXene/conductive polymer and MXene/carbonaceous materials have been examined. Boota *et al.* studied the supercapacitor property of MXene electrode prepared by *in situ* polymerization of

[a]*Artie McFerrin Department of Chemical Engineering, Texas A&M University, College Station, TX 77843, USA. E-mail: micah.green@tamu.edu, jodie.lutkenhaus@tamu.edu*

[b]*Department of Materials Science and Engineering, Texas A&M University, College Station, TX 77843, USA*

†Electronic supplementary information (ESI) available. See DOI: 10.1039/d1nr02114a

pyrrole (PPy).[10] Very high volumetric capacitance of 1000 F cm^{-3} was achieved due to the combined effect of enhanced interlayer spacing between the PPy-intercalated MXene layer and additional surface redox contribution of PPy. The conductive filler plays the role of conductive "bridge" to connect separated $Ti_3C_2T_z$ blocks. Charge storage property of $Ti_3C_2T_z$ also increased by forming hybrid structure of $Ti_3C_2T_z$/CNT and $Ti_3C_2T_z$/rGO.[11] Xu *et al.* prepared graphene/MXene films by vacuum filtration process and achieved remarkably high specific capacitance (405 F g^{-1}) compared to pure MXenes (45 F g^{-1}) and rGO films (282 F g^{-1}).[9] The conductive rGO acts as a bridge between the separated MXene layers; thus electrical conductivity was increased. In addition, rGO sheets inserted between MXene layers prevent agglomeration and allows for fast electrolyte ion transport. However, the specific capacitance of MXene/rGO structure is comparatively lower than other redox/EDLC hybrid electrodes (for example rGO/NiO and rGO MnO_2) due to lack of porosity and low surface area. Both the porosity and surface area can be improved by forming a 3D (gel or foam) structure. Large internal reactive areas can be achieved when 2D sheets are assembled in a macroscopic 3D structure. Moreover, in comparison to 2D sheets/films, 3D morphologies contain more porous structure with interconnected micro-/nanosheets and hierarchical pores.

Here, 3D $Ti_3C_2T_z$/rGO porous gels were prepared by a one-step hydrothermal reaction. $Ti_3C_2T_z$/GO dispersion with different ratios were gelated in stainless steel autoclaves. As expected, hydrothermal treatment of bare GO dispersion can form rGO gel, but the hydrothermal treatment of bare $Ti_3C_2T_z$ cannot produce a gel structure. 3D gels with different $Ti_3C_2T_z$ contents were employed as supercapacitor electrodes, and the resulting properties showed large variation of properties as a function of $Ti_3C_2T_z$ content. Both current response and potential window of the hybrid gels were significantly higher than those of pure rGO gels. Due to the combined effect of EDLC and redox mechanism, $Ti_3C_2T_z$/rGO gel exhibited high specific and areal capacitance with high energy density.

2. Experimental section

2.1. Materials

The elemental powders Titanium (~325 mesh, 99%), aluminum (~325 mesh, 99.5%), and graphite (7–10 micron, 99%) was acquired from Alfa Aesar. Carbon black (Alfa Aesar, 99.9%), and Polyvinylidene fluoride (PVDF) was purchased from alfa Aesar. Commercial GO with concentration of 4 mg ml^{-1} was purchased from MSE Supplies. Carbon Paper (Alfa Aesar) was used for electrode preparation. *N*-Methyl-2-Pyrrolidone (NMP) and H_2SO_4 was purchased from Sigma-Aldrich.

2.2. Experimental methods

2.2.1. MXene nanosheet synthesis. Uniform particle size of MAX phase is prepared by ball milling of in-house synthesized Ti_3AlC_2 powder for 1 h, following procedure described elsewhere.[12,13] After that, the MAX phase powder was mixed with 6 M Hydrochloric acid (HCl) and Lithium Fluoride (LiF) and kept by magnetic stirring at 40 °C for 40 hours. Then the mixture centrifuged at 9000 rpm for 15 min to remove the HF. The sediment was further washed (in water) at 9000 rpm for 15 min to get rid of unwanted HF. Then, the sediment was redisposed into the Dimethyl Sulfoxide (DMSO) and stirred for 20 h (at room temperature) for intercalation. After mixture was further washed with water 2–3 times followed by bath sonication (1 hour) to delaminate the nanosheets. Finally, the mixture centrifuged for 55 min (at 3500 rpm) and $Ti_3C_2T_z$ nanosheets collected from the supernatant. $Ti_3C_2T_z$ nanosheets were freeze dried for 3 days.

2.2.2. Gelation. The freeze-dried $Ti_3C_2T_z$ nanosheets were redispersed by bath-sonication (4 mg ml^{-1}) in water. GO dispersion (4 mg ml^{-1} in water) was added to $Ti_3C_2T_z$ dispersion in different ratios. For every 0.1 M of as-prepared nanosheet dispersion, premixed NaAsc stock solution was added to make 100 ml dispersion with (1 mg ml^{-1} concentration). The GO : $Ti_3C_2T_z$ (G : M) ratio was varied as: GM0 (0 : 100), GM1 (70 : 30), GM2 (50 : 50), GM3 (40 : 60), and GM4 (30 : 70), respectively. The mixture placed in a stainless-steel autoclave and kept in an oven for 20 h at 120 °C. After that, a gel was found for GM0, GM1, GM2, GM3 within transparent water in the autoclave container. However, a gel structure was not formed at higher $Ti_3C_2T_z$ loading (GM4). The gel samples were collected and washed with DI water. After that the sample was kept in a freeze-drier for 24 h and final product was collected.

2.3. Characterization techniques

The surface morphology of the samples was imaged with a scanning electron microscope (SEM, FEI QUANTA 600 FE-SEM) operating at 5 kV accelerating voltage. TEM sample preparation: 5 μL of water dispersion of the Gel (0.5 mg mL^{-1} in water) was drop-casted on a holey carbon grid and the grid was pre-treated by glow-discharging to make it hydrophilic. The excess solution was wiped off and then air-dried. The samples were imaged using a FEI Tecnai Twin (Biology) TEM device operating at 200 kV. Raman spectra of the commercial graphene and EEG were recorded by using a Horiba Jobin–Yvon Lab Ram HR (633 nm) instrument.

2.4. Supercapacitor electrode preparation and measurement

$Ti_3C_2T_z$/rGO gel powder were used as the active material to prepare the supercapacitor electrode. The electrodes are composed of 80 wt% active material, 10 wt% carbon black (Alfa Aesar, 99.9%), and 10 wt% polyvinylidene fluoride (PVDF) binder. The active material, carbon black and binder are dispersed in *N*-Methyl-2-Pyrrolidone (NMP). The supercapacitor electrode is constructed by roll-pressing the dispersion onto a flat carbon paper surface. The electrodes are then dried for 48 h at room temperature. Before electrochemical characterization, the electrodes are immersed in the electrolyte solution for 0.5 h in order to enhance the electrolyte diffusion into the material bulk.

The electrochemical properties of the gels were investigated with cyclic voltammetry (CV), charge–discharge and electrochemical impedance spectroscopy (EIS) by a Gamry Reference 3000™ potentiostat. AgCl and platinum wire was used as reference and as counter electrode, respectively. Symmetric "Swagelok" Type cell constructed by assembling two electrodes and one separator. A Celgard™ separator (3501 Coated PP) is used. The electrolyte is 1 M H_2SO_4.

3. Results and discussion

3.1. Gel preparation

Our approach to create $Ti_3C_2T_z$/rGO hybrids takes the gelation of GO as a starting point.[14] Our intent is to gelate GO with $Ti_3C_2T_z$ present in order to achieve a highly porous structure combining advantages of both nanomaterials. Mixtures of $Ti_3C_2T_z$ nanosheets and GO with different ratios were placed in a stainless-steel autoclave and kept in an oven for 20 h at 120 °C. The GO : $Ti_3C_2T_z$ (G : M) ratio was varied as: GM0 (0 : 100), GM1 (70 : 30), GM2 (50 : 50), GM3 (40 : 60), and GM4 (30 : 70), respectively. The synthesis procedure is described in Fig. 1. After that, a gel was found for GM0, GM1, GM2, GM3 within transparent water in the autoclave container. An optical image of gel (GM2) is shown in Fig. 1. However, a gel structure was not formed at higher $Ti_3C_2T_z$ loading (GM4). This occurs because there is insufficient graphene content to form the interconnected structure; the $Ti_3C_2T_z$ does not participate in the gelation process. Prior work (including our own) has demonstrated similar GO gelation processes under these conditions; when a foreign element (such as $Ti_3C_2T_z$ in our case) is present, it may act as an additional cross-linker and promote gel formation.[15–18] The gel samples were collected, washed, and dried in a freeze-drier for 24 h to obtain the final product.

3.2. Material characterization

Electron microscopy images of the resulting gels are shown in Fig. 2. Nanosheets are visible at high magnifications in the SEM images (Fig. 2a and b). Near-transparent sheets can be seen in the TEM image of GM2 gel (Fig. 2c and d). From the TEM image, overlapping sheets can be seen, such that certain areas show one sheet and other areas show two. Fig. S1† shows a low magnification FE-SEM image of GM2 gel, confirming a highly porous structure. A more crumpled, less porous structure was seen in the FE-SEM image of pure rGO gel (GM0) (Fig. S2†). However, a porous gel structure was observed from the FE-SEM image of GM1 and GM3 (Fig. S3†). Fig. S4† shows the FE-SEM image of $Ti_3C_2T_z$ nanosheets.

EDS analysis was carried out on both GM2 and GM0, with results summarized in Table 1. (This corresponds to SEM images in Fig. S5.†) The GM2 composition was ~38 wt% of Ti, 34 wt% of C and 24 wt% of O. This indicates that GM2 gel contained $Ti_3C_2T_z$ sheets and rGO to form a porous structure. EDS of GM0 shows ~21 wt% O (lower than typical GO values),[19,20] suggesting that the GO is partially reduced during hydrothermal treatment.

XRD was carried out in order to confirm the composition of the GM2 gel (Fig. 3a). XRD pattern shows the presence of peaks corresponding to both rGO and $Ti_3C_2T_z$. The peak at 26° (002) indicates the reduction of GO to rGO during the hydrothermal process. In addition, the appearance of (002) and (104) peaks confirmed the presence of $Ti_3C_2T_z$ in GM2 gel. The formation of rGO/$Ti_3C_2T_z$ gel was further confirmed by Raman spectra analysis. Fig. 3b shows the Raman spectra of GM2. The Raman peak at 624 cm^{-1} was attributed to the characteristic vibrational modes of $Ti_3C_2T_z$. On the other hand, the peaks at 1347 and 1586 cm^{-1} was corresponding to the D and G band of rGO. However, the D band intensity is comparatively high than G band. Previously, EDS analysis shows that GO was not completely reduced during hydrothermal treatment.

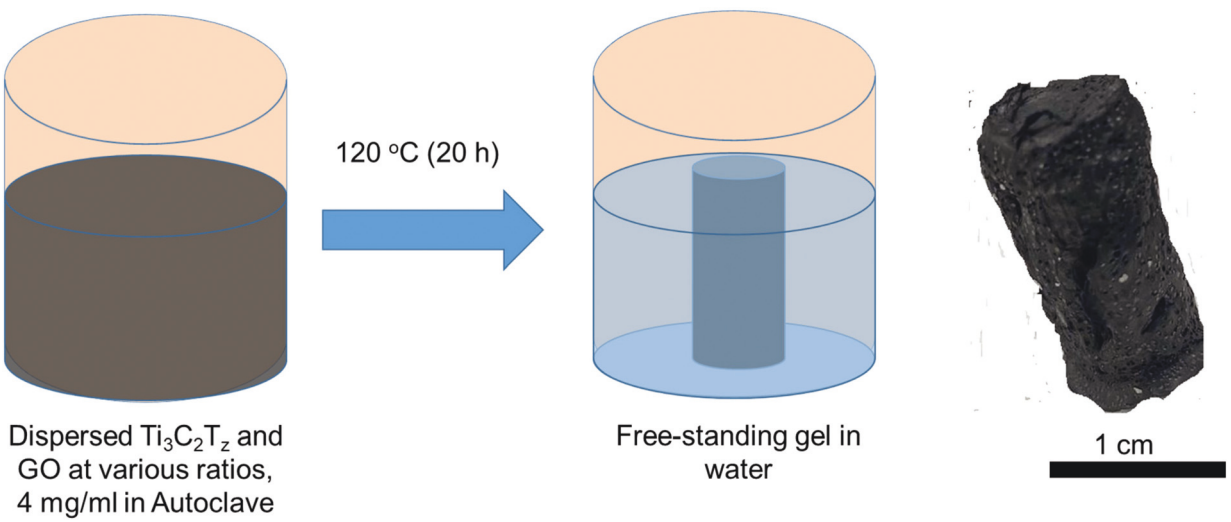

Fig. 1 One-step hydrothermal synthesis process for $Ti_3C_2T_z$/rGO gel. The gel was collected from the autoclave and dried in a freeze-drier for 24 h.

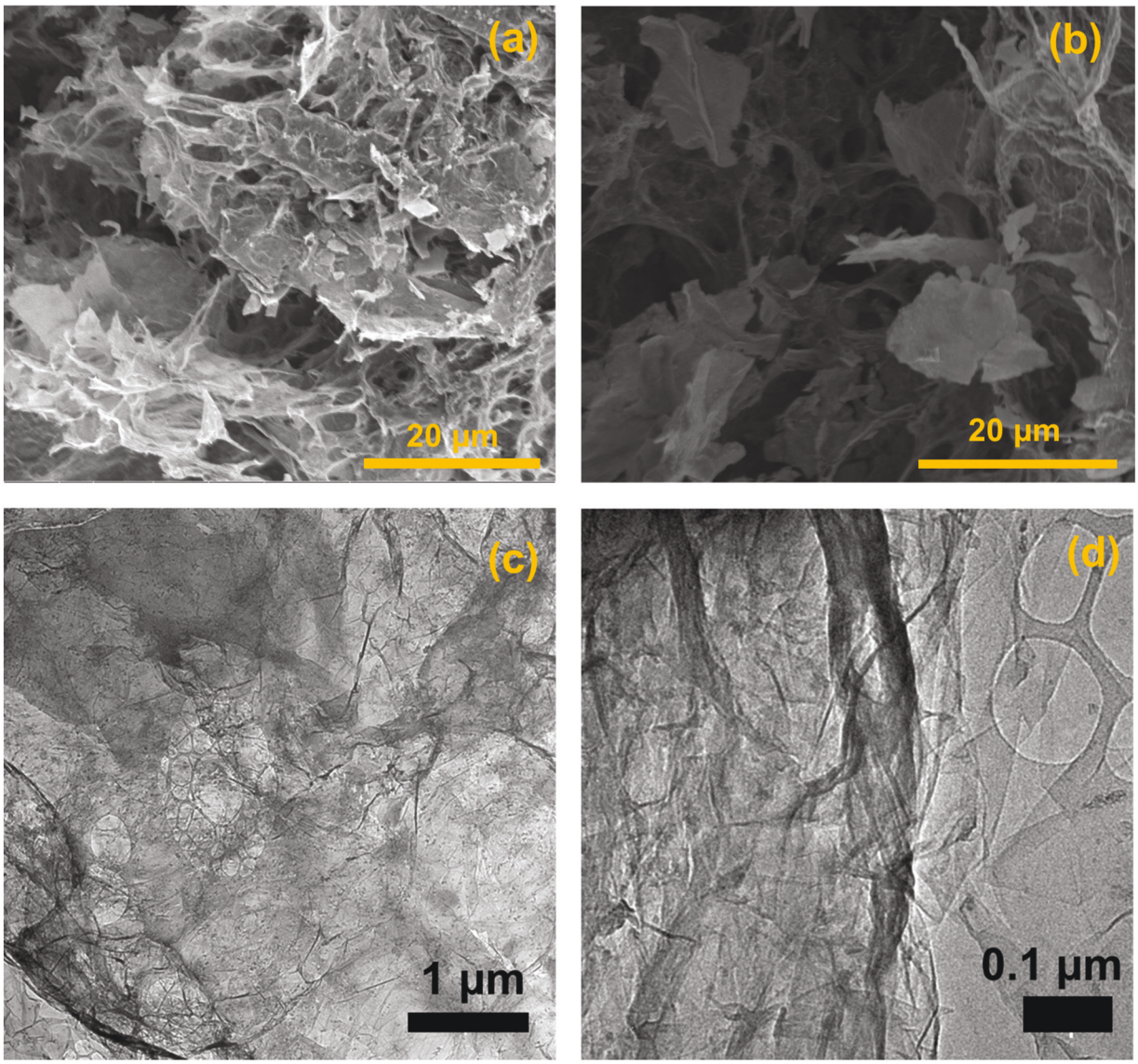

Fig. 2 (a and b) FE-SEM images of GM2 gel and (c and d) TEM image of GM2 gel.

Table 1 EDS analysis results of GM0 and GM2

	Ti (wt%)	C (wt%)	O (wt%)
GM0	—	79.1	20.9
GM2	37.9	34.4	24.3

Remaining oxygen functionalities at the edge of rGO in GM2 gel contribute to the higher D band intensity.

The N_2 adsorption–desorption isotherms are shown in Fig. 4a, while Fig. 4b shows the variation of pore volume with respect to pore diameter of GM2. The BET surface area of GM2 is found to be very high (~224 $m^2\ g^{-1}$). Fig. 4a shows little deviation (the adsorption and desorption do not overlap) in the curve at the higher p/p_0. This kind of upward deviation or IV type isotherm arises due to the presence of mesopores with the pore size ranging from 2–50 nm. Due to the mesoporous structure of the GM2 gel the monolayer–multilayer adsorption happens along with capillary condensation in narrow pores of GM2 gel. The available pore diameter of GM2 varies in the range of 2 nm to 17 nm. The average pore diameter is found to be ~3.6 nm. The pore size is appropriate for the transport of electrolyte ions through the electrode material.

In Table S1,† the surface area of GM2 is compared with other reported graphene-based gels and graphene/MXene gels. As-prepared GM2 has comparatively higher surface area than other reported graphene/MXene gels. However, the surface area of GM2 is lower than the graphene-only gels.

3.3. Electrochemical characterization

The comparison of three electrode CV of GM1, GM2, and GM3 at low (10 mV s^{-1}) scan rate is shown in Fig. 5a. The CV shape

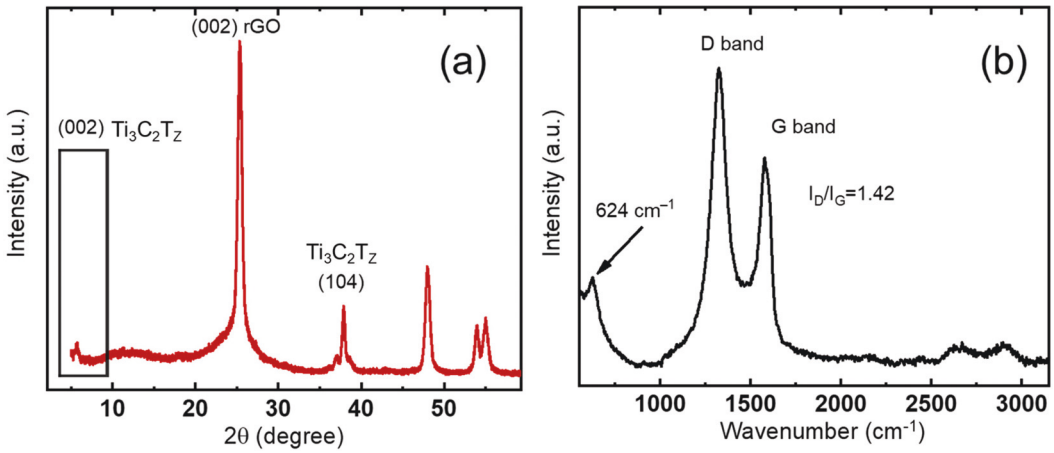

Fig. 3 (a) XRD and (b) Raman spectra of GM2 gel.

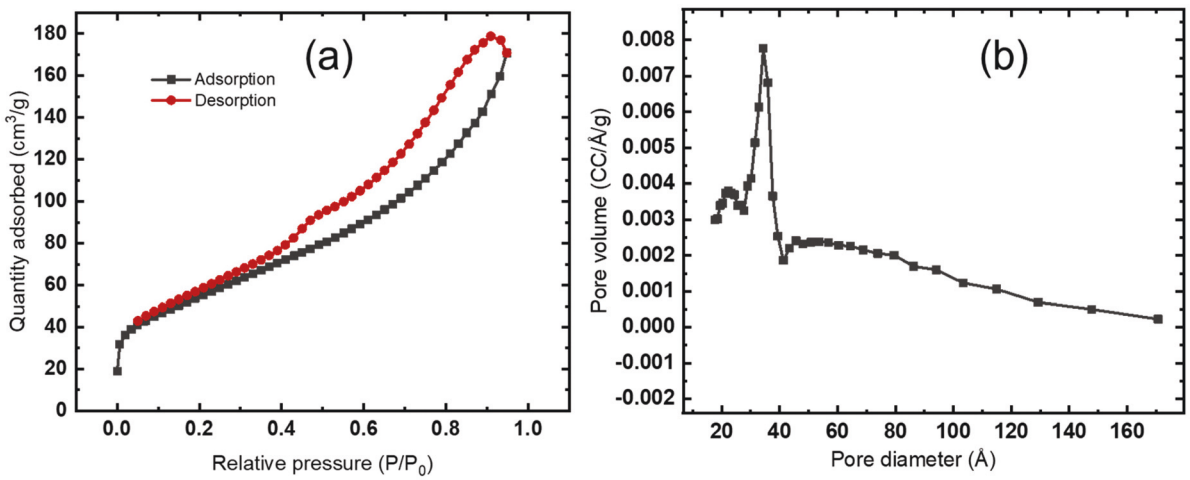

Fig. 4 (a) N_2 adsorption–desorption isotherm and (b) pore volume *vs.* pore size distribution of GM2 gel.

of GM1 is almost EDLC. However small – oxidation and reduction peaks around 0.55 V and 0.45 V are observed. This shape indicates that the capacitance of GM1 is mostly due to EDLC formation, with a small redox contribution. However, GM2 shows prominent oxidation and reduction peaks. In spite of the appearance of redox peak, the nature of the CV is almost undistorted. This indicates that the faradaic capacitance increases with increasing $Ti_3C_2T_z$ content. In spite of increasing faradaic nature, the EDLC contribution of GM2 remains intact. However, the CV of GM3 completely loses its EDLC signature and shows intense redox peaks. This behavior suggests that the charge storage mechanism of GM3 is dominated by redox charge transfer. $Ti_3C_2T_z$/rGO gel contains two different composition $Ti_3C_2T_z$ and rGO. Here, rGO contributes *via* EDLC mechanisms whereas $Ti_3C_2T_z$ takes part in redox reaction. When the composition is varied, the relative content of EDLC and redox capacitance also varied. Redox mechanism has higher charge storage capacity than EDLC. As a result, with increasing rGO content, the specific capacitance of $Ti_3C_2T_z$ gel increased significantly. On the other hand, EDLC has higher retention capability. Thus, at very high content of $Ti_3C_2T_z$ the retention of specific capacitance decreased.

The three electrode CV performance of GM1, GM2, and GM3 at high (10 mV s^{-1}) scan rate is shown in Fig. 5b. At high scan rates, all the sample lost their corresponding redox peaks, suggesting that the redox charge transfer did not take place at very fast charge–discharge rates. At higher scan rate, the Redox reaction time is slower compared to the fast scan rate. Thus, not all the redox active sites could take part to the charge transfer process. As a result, redox peaks disappear at higher scan rate. In addition, the CV nature of GM3 becomes completely distorted at high scan rates. This is due to the fact that at high scan rates, the electrolyte ions were not able to access all the active site of the electrode material. Thus, it can be concluded that higher $Ti_3C_2T_z$ content increased the charge storage capacity, but also deteriorates the charge transfer rate of the gel electrode.

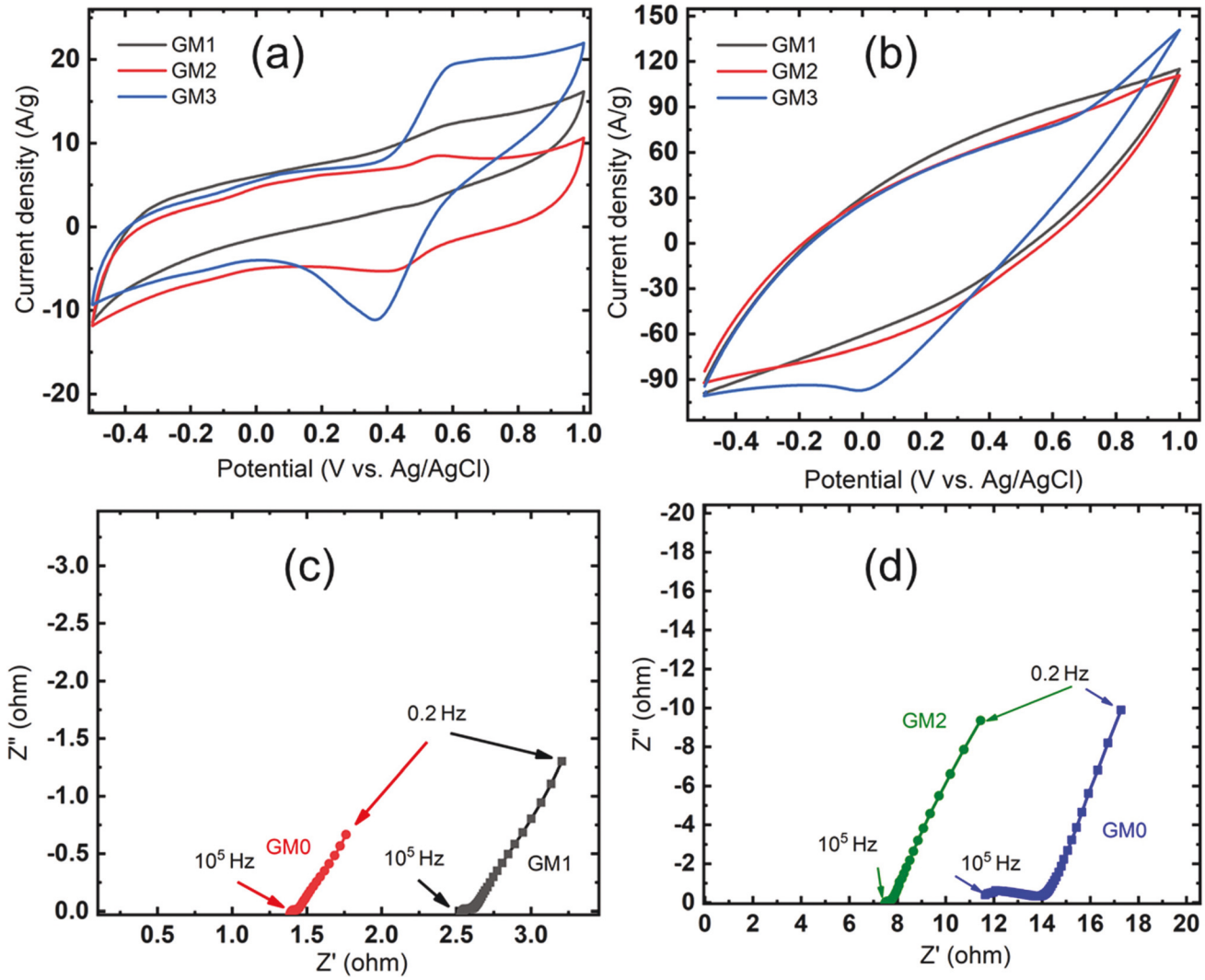

Fig. 5 CV at (a) 10 mV s^{-1} and (b) 500 mV s^{-1} of GM1, GM2 and GM3, Nyquist plot of EIS results of (c) GM0 and GM1, and (d) GM2 and GM3. Ag/AgCl and platinum wire are used as references and counter electrode, respectively.

The three electrode CV of pure rGO gel (GM0), $Ti_3C_2T_z$ nanosheets and $Ti_3C_2T_z$/rGO gel (GM2) are compared in Fig. S6† at 10 mV s^{-1} scan rate. The specific capacitance was calculated as 314, 402 and 920 F g^{-1} for GM0, MXene nanosheets and GM2, respectively. The specific capacitance of $Ti_3C_2T_z$/rGO is much larger than those of both the pure rGO and $Ti_3C_2T_z$ nanosheets. The combined effect of EDLC and faradaic capacitance is the reason for high capacitance in $\mathbf{Ti_3C_2T_z}$ MXene/rGO gel. The specific capacitance of the present work ($Ti_3C_2T_z$/rGO gel) was also compared with previously reported pure rGO, graphene and $\mathbf{Ti_3C_2T_z}$ MXene electrodes in Table S2.†[21–28] The specific capacitance of $Ti_3C_2T_z$/rGO gel is significantly higher than those of pure rGO and $\mathbf{Ti_3C_2T_z}$ MXene electrodes. Thus, it can be concluded from Table S2† that hybridization of $Ti_3C_2T_z$ and rGO is a better choice when compared to pure rGO or $\mathbf{Ti_3C_2T_z}$ MXene electrodes. Fig. S7† shows the CV of GM0, GM1, GM2 and GM3 at various scan rates. The potential window of $Ti_3C_2T_z$ content gel electrode (GM1, GM2 and GM3) was 1.5 V (−0.5 to 1 V). However, the pure rGO gel electrode (GM0) exhibits a relatively small potential window of 1 V (−0.5 to 0.5 V). In addition, rGO gel shows complete EDLC nature. With increasing scan rate, the current response increased for all the gel electrodes. Table 2 compares the CV performance of GM0, GM1, GM2 and GM3. At 10 mV

Table 2 Specific capacitance of GM0, GM1, GM2 and GM3 at various scan rates

	Specific capacitance (F g^{-1})			
Scan rate (mV s^{-1})	GM0	GM1	GM2	GM3
10	314	701	920	1100
50	208	546	549	747
100	132	433	401	422
200	81	281	275	297
500	62	140	142	140

s^{-1} scan rate. The specific capacitance of GM0, GM1, GM2 and GM3 at 10 mV s^{-1} scan rate was measured to be 314, 701, 920 and 1100 F g^{-1} respectively. The specific capacitance increases significantly with increasing $Ti_3C_2T_z$ content. However, specific capacitance of higher $Ti_3C_2T_z$ content sample was comparatively poor at higher scan rate. The specific capacitance of GM0, GM1, GM2, and GM3 at 500 mV s^{-1} scan rate was measured to be 62, 140, 142, and 140 F g^{-1} respectively. The retention (at 500 mV s^{-1} scan rate) was ~20%, 20%, 15% and 13% for GM0, GM1, GM2, and GM3, respectively.

The Nyquist plots of GM0, GM1, GM2 and GM3 are presented in Fig. 5c and d. The EIS measurement was carried out in a frequency range of 0.2 to 10^5 Hz. The series resistance increased significantly with increasing $Ti_3C_2T_z$ content. The series resistance of GM0, GM1, GM2, and GM3 was measured as 1.3, 2.5, 7.8, and 11.6 Ohm, respectively. Comparatively large faradaic resistance (~1.5 Ohm) of GM3 suggests the existence of high charge transfer resistance during charging–discharging. The gel contains two different components, $Ti_3C_2T_z$ and rGO. Here, rGO contributes *via* the EDLC mechanism, and $Ti_3C_2T_z$ takes part in a redox reaction. It is interesting to note that even with increasing $Ti_3C_2T_z$ content, the charge transfer resistance increases. For rGO, electrostatic charge separation at electrode/electrolyte interface is the origin of capacitance, and no charge transfer resistance arises. However, for $Ti_3C_2T_z$, the redox potential of electrode and electrolyte are different. As a result, a potential barrier arises at the electrode/electrolyte interface.[29,30] This potential barrier is the characteristic of electrode material and corresponding electrolyte. Here, with increasing Ti_3C_2Tz content in the gel, the contribution of EDLC decreases and contribution of redox capacitance increases. Thus, due to the presence of higher amount of redox active material, the charge transfer resistance increases due to increasing potential barriers at the electrode electrolyte interface.

The variation of the voltammetric charge (q^*) with respect to the sweep rates v: extrapolation of q^* to $v = \infty$ from the q^* *versus* $1/v^{1/2}$ plot is presented in Fig. 6a. The intersection is correlated with the available active sites on the exposed surface of the electrode material. If the amount of active site on the exposed surface increases then the supercapacitor can maintain its higher capacitance value during fast charge–discharge. Thus, charge storage capability increases with these active electrode sites. The outer active site was estimated as 41, 206, 108, and 97 C g^{-1} for GM0, GM1, GM2, and GM3, respectively. It was interesting to notice that GM1 has more outer active sites than GM0. This shows that initially with the introduction of $Ti_3C_2T_z$ the outer charge storage capability of the electrode increases. However, with further increasing $Ti_3C_2T_z$ content the amount of outer active sites decreased. This behavior suggested that increased content of $Ti_3C_2T_z$ actually decreases the outer charge storage capability.

The Mott–Schottky plots of GM1, GM2 and GM3 are shown in Fig. 6b. Due to the presence of two different kind of materials ($Ti_3C_2T_z$ and zero bandgap rGO), $Ti_3C_2T_z$/rGO gels behave like semiconducting material. The data indicates that a potential barrier developed at the electrode electrolyte interface when the two come in to contact. This potential barrier is the origin of the redox charge transfer among the active sit of electrode and electrolyte ions. The positive slope of the Mott–Schottky plot indicates the n-type semiconducting nature of the GM samples. The inverse of the slope is proportional to the defect (charge active site) density. The active site density in GM3 is much higher. This is the reason for high redox capacitance in GM3.

A symmetric supercapacitor cell was prepared by using GM2 as the electrode material. The area of electrode is ~0.785 cm^2. The CV nature (Fig. 7a) shows an EDLC-like signature, and a large potential window of 1.2 V was achieved. A high areal capacitance of 560 mF cm^{-2} was achieved at 10 mV s^{-1} scan rate. Fig. 7b shows the charge–discharge of GM2 supercapacitor cell at various current density. The areal capacitance was measured to be 158, 133, 106, and 76 mF cm^{-2} at current density of 0.6, 1.3, 5.1, and 10.2 mA cm^{-2}, respectively.

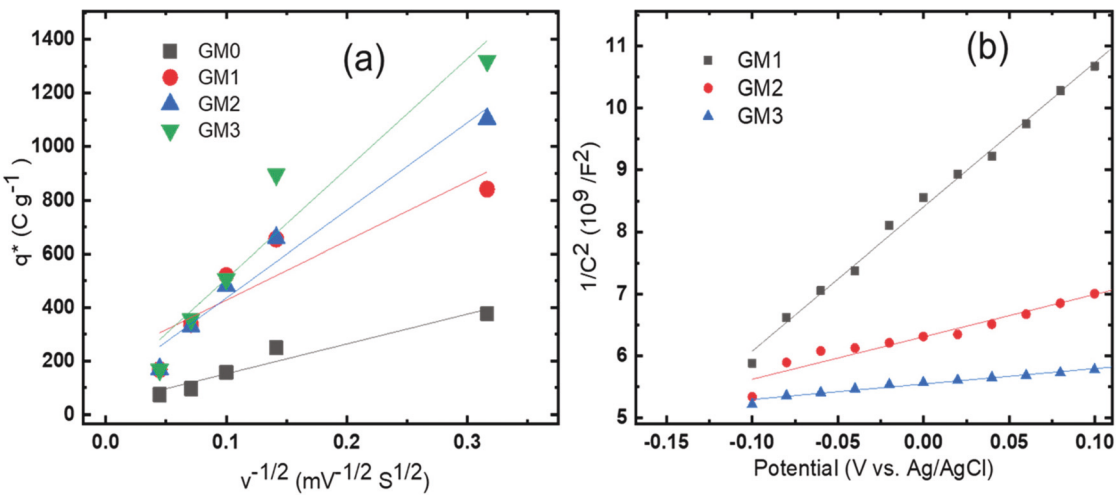

Fig. 6 (a) Variation of the voltammetric charge (q^*) with respect to the scan rates (v); the lines indicate a linear fit; and (b) Mott–Schottky plot (variation of $1/C^2$ *vs.* V).

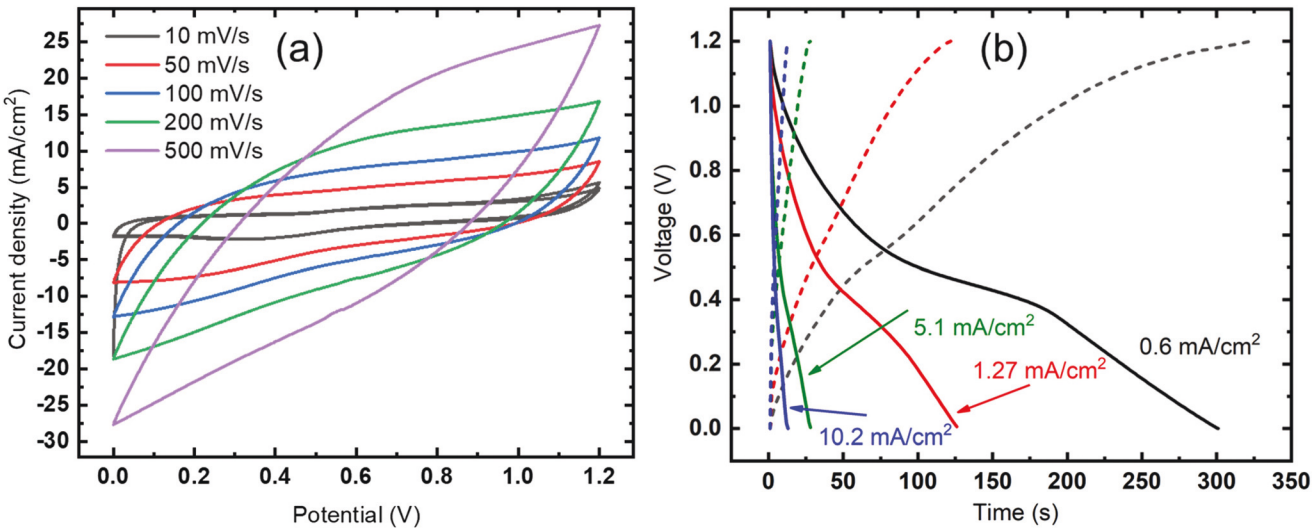

Fig. 7 Two electrode (a) CV and (b) CD of GM2 at various scan rates and current density (dotted line represented charging and continuous line for discharging).

CD curves for GM0, GM1 and GM3 at various current density values is represented in Fig. S8.† CD curves show that the charge storage mechanism of the gel supercapacitor is not completely capacitive but also diffusive in nature. The areal capacitance of GM0, GM1, GM2, and GM3 symmetric cell was summarized in Table 3. Although, the specific capacitance (three electrode) of GM3 was higher than GM2, but the areal capacitance of GM3 is much lower than GM2. It suggested that due to the faradaic nature of GM3 as well as lower voltammetric charge density GM3 shows poor charge storage performance when employed in symmetric cell. coulombic efficiency, which is the ratio of discharging and charging time, is another parameter to evaluate the supercapacitor performance. In ideal case, the coulombic efficiency is 100%, *i.e.* charging and discharging time is equal. However, in practical the entire charge transfer reaction are not completely reversible and discharging time is generally lower than charging time. The symmetric supercapacitors also exhibited high coulombic efficiency (calculated from the CD plots). GM0 shows highest coulombic efficiency of 97 and 98% at 0.6 and 1.3 mA cm^{-2} current density. As the charge storage mechanism of GM0 is EDLC and no redox type materials is present, the coulombic efficiency is very high. The coulombic efficiency of GM1, GM2, and GM3 are low compared to GM0 due to the presence of $Ti_3C_2T_z$. The coulombic efficiency was calculated as ~93, 94 and 94% for GM1, GM2, and GM3 respectively, at 0.6 mA cm^{-2} current density. On the other hand, at 1.3 mA cm^{-2} current density, the coulombic efficiency was 97% for all the supercapacitor tests (GM1, GM2 and GM3).

Fig. S9† shows the Ragone plot of GM0, GM, GM2, and GM3 two-electrode supercapacitor cell and the corresponding results were summarized in Table 4. The highest measured energy density (31.5 μW h cm^{-2}) was achieved at a power density of 370 μW cm^{-2}. At very high-power density of 6120 μW cm^{-2}, the energy density remained high at ~22.1 μW h cm^{-2}. The supercapacitor property (areal capacitance, energy and power density, and stability) of the present work was compared with previously reported pure $\mathbf{Ti_3C_2T_z}$ MXene, pure rGO and different hybrid MXene and rGO symmetric supercapacitor in Table S3.† [31–40] It was found that $Ti_3C_2T_z$/rGO gel possess comparable and, in some cases, significantly better supercapacitor performance compared to other reported materials. Fig. S10† shows the performance of GM2 two-electrode supercapacitor for 10 000 cycles, confirming a high (~93%) cycling stability. The stability was measured at a current density of 5.1 mA cm^{-2}. After 10 000 cycles, no significant cracking or morphological change was observed. An FE-SEM image (Fig. S11†) of GM2 gel after 10 000 cycles shows a highly porous structure, similar to the un-used $Ti_3C_2T_z$/rGO. This suggests that the gel

Table 3 Areal capacitance (at different current density) of GM0, GM1, GM2, and GM3 symmetric device

	Areal capacitance (mF cm^{-2})			
Current density (mA cm^{-2})	GM0	GM1	GM2	GM3
0.6	59	65	158	108
1.3	49	53	140	69
5.1	40	43	127	59
10.2	30	34	110	42

Table 4 Energy density (at different power density) of GM0, GM1, GM2 and GM3 symmetric device

	Energy density (μW h cm^{-2})			
Power density (μW cm^{-2})	GM0	GM1	GM2	GM3
370	8.2	12.9	31.5	21.6
760	6.2	10.6	28.6	11.6
3000	5.7	9.4	25.5	9.4
6120	4.3	8.5	22.1	8.5

structure formed by one-step hydrothermal process is suitable for long life and stable supercapacitor applications.

4. Conclusions

The results of this study show that hybridization of $Ti_3C_2T_z$ and rGO and formation of porous structure can significantly improve electrochemical energy storage performance of the respective nanomaterials. $Ti_3C_2T_z$/rGO gel was prepared by one-step hydrothermal process. There are few previous reports on the preparation of $Ti_3C_2T_z$/rGO gel; however, they used anti-oxidants during synthesis. We prepared the $Ti_3C_2T_z$/rGO gels without using any anti-oxidant. In addition, no other reducing agent was used during the synthesis process. Reduction of GO to rGO and formation of $Ti_3C_2T_z$/rGO gel was performed in a single step through an appropriate temperature and time for the hydrothermal reaction. This is important because with higher temperature or longer times, $\mathbf{Ti_3C_2T_z}$ MXenes can be oxidized, while at lower temperature and times, gel formation is not possible. Furthermore, the supercapacitor performance of the present material is also higher (Tables S2 and S3†) than other reported MXene/rGO gels.[22,24,25,28,32,37,41–52] The $Ti_3C_2T_z$/rGO gels consisted of nanosheets in a highly porous structure with a surface area of ~224 $m^2\ g^{-1}$ and average pore diameter of ~3.6 nm. $Ti_3C_2T_z$/rGO gel with different compositions was employed as supercapacitor electrodes. All $Ti_3C_2T_z$/rGO gel electrodes show larger potential window and high specific capacitance than the pure rGO gel and $Ti_3C_2T_z$. The synergistic effect of EDLC from rGO and redox capacitance from $Ti_3C_2T_z$ allows for enhanced supercapacitor performance of $Ti_3C_2T_z$/rGO gels. Higher $Ti_3C_2T_Z$ content increased the specific capacitance but decreased the retention value at higher scan rates. The gel structure with equivalent GO and $Ti_3C_2T_Z$ content shows the best supercapacitor performance, with high capacitance as well as excellent retention. Compared to other rGO and $Ti_3C_2T_z$ based hybrid electrodes in the literature, our porous $Ti_3C_2T_z$/rGO gels exhibited superior supercapacitor properties. $Ti_3C_2T_z$/rGO gel showed very high energy density of ~31.5 μW h cm^{-2} corresponding to a power density of ~370 μW cm^{-2}. Due to the highly porous structure and appropriate content of $Ti_3C_2T_z$ and rGO, $Ti_3C_2T_z$/rGO gel also maintain a high energy density (~22.1 μW h cm^{-2}) corresponding a very high-power density of 6120 μW cm^{-2}. The coulombic efficiency of the supercapacitor also very high (~94%) even at lower current density of 0.6 mA cm^{-2}. In addition, $Ti_3C_2T_z$/rGO symmetric cell also exhibited stable performance, with ~93% retention after 10 000 cycles. Large areal capacitance at high current density and large energy storage capacity even at high power density indicates that $Ti_3C_2T_z$/rGO gels are highly promising for energy storage applications.

Conflicts of interest

There are no conflicts to declare.

Acknowledgements

This work was supported by the US National Science Foundation (grant CMMI-1760859). Use of the TAMU Materials and Characterization Facility and assistance of Dr Wilson Serem are acknowledged.

References

1 S. Chu and A. Majumdar, Opportunities and challenges for a sustainable energy future, *Nature*, 2012, **488**, 294–303.
2 Y. Wang, Y. Song and Y. Xia, Electrochemical capacitors: mechanism, materials, systems, characterization and applications, *Chem. Soc. Rev.*, 2016, **45**, 5925–5950.
3 K. Zhu, Y. Jin, F. Du, S. Gao, Z. Gao, X. Meng, G. Chen, Y. Wei and Y. Gao, Synthesis of Ti2CTx MXene as electrode materials for symmetric supercapacitor with capable volumetric capacitance, *J. Energy Chem.*, 2019, **31**, 11–18.
4 M. Hu, H. Zhang, T. Hu, B. Fan, X. Wang and Z. Li, Emerging 2D MXenes for supercapacitors: status, challenges and prospects, *Chem. Soc. Rev.*, 2020, **49**, 6666–6693.
5 M. R. Lukatskaya, S.-M. Bak, X. Yu, X.-Q. Yang, M. W. Barsoum and Y. Gogotsi, Probing the Mechanism of High Capacitance in 2D Titanium Carbide Using In Situ X-Ray Absorption Spectroscopy, *Adv. Energy Mater.*, 2015, **5**, 1500589.
6 M. Hu, Z. Li, T. Hu, S. Zhu, C. Zhang and X. Wang, High-Capacitance Mechanism for Ti3C2Tx MXene by in Situ Electrochemical Raman Spectroscopy Investigation, *ACS Nano*, 2016, **10**, 11344–11350.
7 M. R. Lukatskaya, O. Mashtalir, C. E. Ren, Y. Dall'Agnese, P. Rozier, P. L. Taberna, M. Naguib, P. Simon, M. W. Barsoum and Y. Gogotsi, Cation Intercalation and High Volumetric Capacitance of Two-Dimensional Titanium Carbide, *Science*, 2013, **341**, 1502–1505.
8 M. S. Javed, H. Lei, H. U. Shah, S. Asim, R. Raza and W. Mai, Achieving high rate and high energy density in an all-solid-state flexible asymmetric pseudocapacitor through the synergistic design of binder-free 3D $ZnCo_2O4$ nano polyhedra and 2D layered Ti3C2Tx-MXenes, *J. Mater. Chem. A*, 2019, **7**, 24543–24556.
9 S. Xu, G. Wei, J. Li, W. Han and Y. Gogotsi, Flexible MXene–graphene electrodes with high volumetric capacitance for integrated co-cathode energy conversion/storage devices, *J. Mater. Chem. A*, 2017, **5**, 17442–17451.
10 M. Boota, B. Anasori, C. Voigt, M.-Q. Zhao, M. W. Barsoum and Y. Gogotsi, Pseudocapacitive Electrodes Produced by Oxidant-Free Polymerization of Pyrrole between the Layers of 2D Titanium Carbide (MXene), *Adv. Mater.*, 2016, **28**, 1517–1522.
11 M.-Q. Zhao, C. E. Ren, Z. Ling, M. R. Lukatskaya, C. Zhang, K. L. Van Aken, M. W. Barsoum and Y. Gogotsi, Flexible MXene/Carbon Nanotube Composite Paper with High Volumetric Capacitance, *Adv. Mater.*, 2015, **27**, 339–345.

12 X. Zhao, A. Vashisth, E. Prehn, W. Sun, S. A. Shah, T. Habib, Y. Chen, Z. Tan, J. L. Lutkenhaus, M. Radovic and M. J. Green, Antioxidants Unlock Shelf-Stable Ti3C2Tx (MXene) Nanosheet Dispersions, *Matter*, 2019, **1**(2), 513–526.

13 X. Zhao, A. Vashisth, J. W. Blivin, Z. Tan, D. E. Holta, V. Kotasthane, S. A. Shah, T. Habib, S. Liu, J. L. Lutkenhaus, M. Radovic and M. J. Green, pH, Nanosheet Concentration, and Antioxidant Affect the Oxidation of Ti3C2Tx and Ti2CTx MXene Dispersions, *Adv. Mater. Interfaces*, 2020, **7**, 2000845.

14 K. Hu, X. Xie, T. Szkopek and M. Cerruti, Understanding Hydrothermally Reduced Graphene Oxide Hydrogels: From Reaction Products to Hydrogel Properties, *Chem. Mater.*, 2016, **28**, 1756–1768.

15 H. Bai, C. Li, X. Wang and G. Shi, On the Gelation of Graphene Oxide, *J. Phys. Chem. C*, 2011, **115**, 5545–5551.

16 W. Ai, Z.-Z. Du, J.-Q. Liu, F. Zhao, M.-D. Yi, L.-H. Xie, N.-E. Shi, Y.-W. Ma, Y. Qian, Q.-L. Fan, T. Yu and W. Huang, Formation of graphene oxide gel via the π-stacked supramolecular self-assembly, *RSC Adv.*, 2012, **2**, 12204–12209.

17 D. Parviz, S. A. Shah, M. G. B. Odom, W. Sun, J. L. Lutkenhaus and M. J. Green, Tailored Network Formation in Graphene Oxide Gels, *Langmuir*, 2018, **34**, 8550–8559.

18 S. A. Shah, D. Kulhanek, W. Sun, X. Zhao, S. Yu, D. Parviz, J. L. Lutkenhaus and M. J. Green, Aramid nanofiber-reinforced three-dimensional graphene hydrogels for supercapacitor electrodes, *J. Colloid Interface Sci.*, 2020, **560**, 581–588.

19 S. W. Lee, C. Mattevi, M. Chhowalla and R. M. Sankaran, Plasma-Assisted Reduction of Graphene Oxide at Low Temperature and Atmospheric Pressure for Flexible Conductor Applications, *J. Phys. Chem. Lett.*, 2012, **3**, 772–777.

20 R. Rozada, J. I. Paredes, M. J. López, S. Villar-Rodil, I. Cabria, J. A. Alonso, A. Martínez-Alonso and J. M. D. Tascón, From graphene oxide to pristine graphene: revealing the inner workings of the full structural restoration, *Nanoscale*, 2015, **7**, 2374–2390.

21 Z. J. Li, B. C. Yang, S. R. Zhang and C. M. Zhao, Graphene oxide with improved electrical conductivity for supercapacitor electrodes, *Appl. Surf. Sci.*, 2012, **258**, 3726–3731.

22 J. Yan, J. Liu, Z. Fan, T. Wei and L. Zhang, High-performance supercapacitor electrodes based on highly corrugated graphene sheets, *Carbon*, 2012, **50**, 2179–2188.

23 A. M. Obeidat, V. Luthra and A. C. Rastogi, Solid-state graphene-based supercapacitor with high-density energy storage using ionic liquid gel electrolyte: electrochemical properties and performance in storing solar electricity, *J. Solid State Electrochem.*, 2019, **23**, 1667–1683.

24 Y. Li, M. Van Zijll, S. Chiang and N. Pan, KOH modified graphene nanosheets for supercapacitor electrodes, *J. Power Sources*, 2011, **196**, 6003–6006.

25 W. Chen, D. Gui, C. Liu, W. Xiong, X. Cai, G. Tan, S. Li and J. Liu, Preparation of graphene aerogel and its electrochemical properties as the electrode materials for supercapacitors, 2015 16th International Conference on Electronic Packaging Technology (ICEPT), 2015, pp. 35–38.

26 M. Ghidiu, M. R. Lukatskaya, M. Q. Zhao, Y. Gogotsi and M. W. Barsoum, Conductive two-dimensional titanium carbide 'clay' with high volumetric capacitance, *Nature*, 2014, **516**, 78–81.

27 X. Zang, J. Wang, Y. Qin, T. Wang, C. He, Q. Shao, H. Zhu and N. Cao, Enhancing Capacitance Performance of Ti3C2Tx MXene as Electrode Materials of Supercapacitor: From Controlled Preparation to Composite Structure Construction, *Nano-Micro Lett.*, 2020, **12**, 77.

28 Y. Dall'Agnese, M. R. Lukatskaya, K. M. Cook, P.-L. Taberna, Y. Gogotsi and P. Simon, High capacitance of surface-modified 2D titanium carbide in acidic electrolyte, *Electrochem. Commun.*, 2014, **48**, 118–122.

29 S. Srinivasan, Electrode/electrolyte interfaces: Structure and kinetics of charge transfer, in *Fuel Cells*, Springer, 2006, pp. 27–92.

30 X. Zheng, X. Yan, Y. Sun, Z. Bai, G. Zhang, Y. Shen, Q. Liang and Y. Zhang, Au-Embedded ZnO/NiO Hybrid with Excellent Electrochemical Performance as Advanced Electrode Materials for Supercapacitor, *ACS Appl. Mater. Interfaces*, 2015, **7**, 2480–2485.

31 Y. Wang, Y. Zhang, J. Liu, G. Wang, F. Pu, A. Ganesh, C. Tang, X. Shi, Y. Qiao, Y. Chen, H. Liu, C. Kong and L. Li, Boosting areal energy density of 3D printed all-solid-state flexible microsupercapacitors via tailoring graphene composition, *Energy Storage Mater.*, 2020, **30**, 412–419.

32 G. K. Veerasubramani, K. Krishnamoorthy, P. Pazhamalai and S. J. Kim, Enhanced electrochemical performances of graphene based solid-state flexible cable type supercapacitor using redox mediated polymer gel electrolyte, *Carbon*, 2016, **105**, 638–648.

33 L. Kou, T. Huang, B. Zheng, Y. Han, X. Zhao, K. Gopalsamy, H. Sun and C. Gao, Coaxial wet-spun yarn supercapacitors for high-energy density and safe wearable electronics, *Nat. Commun.*, 2014, **5**, 3754.

34 W. Yang, J. Yang, J. J. Byun, F. P. Moissinac, J. Xu, S. J. Haigh, M. Domingos, M. A. Bissett, R. A. W. Dryfe and S. Barg, 3D Printing of Freestanding MXene Architectures for Current-Collector-Free Supercapacitors, *Adv. Mater.*, 2019, **31**, 1902725.

35 C. Zhang, L. McKeon, M. P. Kremer, S.-H. Park, O. Ronan, A. Seral-Ascaso, S. Barwich, C.Ó Coileáin, N. McEvoy, H. C. Nerl, B. Anasori, J. N. Coleman, Y. Gogotsi and V. Nicolosi, Additive-free MXene inks and direct printing of micro-supercapacitors, *Nat. Commun.*, 2019, **10**, 1795.

36 N. Wang, J. Liu, Y. Zhao, M. Hu, R. Qin and G. Shan, Laser-Cutting Fabrication of Mxene-Based Flexible Micro-Supercapacitors with High Areal Capacitance, *ChemNanoMat*, 2019, **5**, 658–665.

37 S. Xu, Y. Dall'Agnese, G. Wei, C. Zhang, Y. Gogotsi and W. Han, Screen-printable microscale hybrid device based

on MXene and layered double hydroxide electrodes for powering force sensors, *Nano Energy*, 2018, **50**, 479–488.

38 Q. Zhang, X. Wang, Z. Pan, J. Sun, J. Zhao, J. Zhang, C. Zhang, L. Tang, J. Luo, B. Song, Z. Zhang, W. Lu, Q. Li, Y. Zhang and Y. Yao, Wrapping Aligned Carbon Nanotube Composite Sheets around Vanadium Nitride Nanowire Arrays for Asymmetric Coaxial Fiber-Shaped Supercapacitors with Ultrahigh Energy Density, *Nano Lett.*, 2017, **17**, 2719–2726.

39 R. N, K. A, M. HM, N. MR, D. Mondal, S. K. Nataraj and D. Ghosh, Binder free self-standing high performance supercapacitive electrode based on graphene/titanium carbide composite aerogel, *Appl. Surf. Sci.*, 2019, **481**, 892–899.

40 Y. Yue, N. Liu, Y. Ma, S. Wang, W. Liu, C. Luo, H. Zhang, F. Cheng, J. Rao, X. Hu, J. Su and Y. Gao, Highly Self-Healable 3D Microsupercapacitor with MXene–Graphene Composite Aerogel, *ACS Nano*, 2018, **12**, 4224–4232.

41 Z. Li, B. Yang, S. Zhang and C. Zhao, Graphene oxide with improved electrical conductivity for supercapacitor electrodes, *Appl. Surf. Sci.*, 2012, **258**, 3726–3731.

42 A. M. Obeidat, V. Luthra and A. Rastogi, Solid-state graphene-based supercapacitor with high-density energy storage using ionic liquid gel electrolyte: electrochemical properties and performance in storing solar electricity, *J. Solid State Electrochem.*, 2019, **23**, 1667–1683.

43 M. Ghidiu, M. R. Lukatskaya, M.-Q. Zhao, Y. Gogotsi and M. W. Barsoum, Conductive two-dimensional titanium carbide 'clay'with high volumetric capacitance, *Nature*, 2014, **516**, 78–81.

44 X. Zang, J. Wang, Y. Qin, T. Wang, C. He, Q. Shao, H. Zhu and N. Cao, Enhancing capacitance performance of Ti 3 C 2 T x MXene as electrode materials of supercapacitor: from controlled preparation to composite structure construction, *Nano-Micro Lett.*, 2020, **12**, 1–24.

45 Y. Wang, Y. Zhang, J. Liu, G. Wang, F. Pu, A. Ganesh, C. Tang, X. Shi, Y. Qiao and Y. Chen, Boosting areal energy density of 3D printed all-solid-state flexible microsupercapacitors via tailoring graphene composition, *Energy Storage Mater.*, 2020, **30**, 412–419.

46 L. Kou, T. Huang, B. Zheng, Y. Han, X. Zhao, K. Gopalsamy, H. Sun and C. Gao, Coaxial wet-spun yarn supercapacitors for high-energy density and safe wearable electronics, *Nat. Commun.*, 2014, **5**, 1–10.

47 W. Yang, J. Yang, J. J. Byun, F. P. Moissinac, J. Xu, S. J. Haigh, M. Domingos, M. A. Bissett, R. A. Dryfe and S. Barg, 3D printing of freestanding MXene architectures for current–collector–free supercapacitors, *Adv. Mater.*, 2019, **31**, 1902725.

48 C. J. Zhang, L. McKeon, M. P. Kremer, S.-H. Park, O. Ronan, A. Seral-Ascaso, S. Barwich, C.Ó Coileáin, N. McEvoy and H. C. Nerl, Additive-free MXene inks and direct printing of micro-supercapacitors, *Nat. Commun.*, 2019, **10**, 1–9.

49 N. Wang, J. Liu, Y. Zhao, M. Hu, R. Qin and G. Shan, Laser–cutting fabrication of MXene–based flexible micro–supercapacitors with high areal capacitance, *ChemNanoMat*, 2019, **5**, 658–665.

50 Q. Zhang, X. Wang, Z. Pan, J. Sun, J. Zhao, J. Zhang, C. Zhang, L. Tang, J. Luo and B. Song, Wrapping aligned carbon nanotube composite sheets around vanadium nitride nanowire arrays for asymmetric coaxial fiber-shaped supercapacitors with ultrahigh energy density, *Nano Lett.*, 2017, **17**, 2719–2726.

51 N. Radha, A. Kanakaraj, H. Manohar, M. Nidhi, D. Mondal, S. K. Nataraj and D. Ghosh, Binder free self-standing high performance supercapacitive electrode based on graphene/titanium carbide composite aerogel, *Appl. Surf. Sci.*, 2019, **481**, 892–899.

52 Y. Yue, N. Liu, Y. Ma, S. Wang, W. Liu, C. Luo, H. Zhang, F. Cheng, J. Rao and X. Hu, Highly self-healable 3D microsupercapacitor with MXene–graphene composite aerogel, *ACS Nano*, 2018, **12**, 4224–4232.